Class E/EF Inductive Power Transfer to Achieve Stable Output under Variable Low Coupling

Yifan Zhao[1], Mowei Lu[1], Heyuan Li[2], Zhenbin Zhang[3], Minfan Fu[2] and Stefan M. Goetz[1]*
[1] *Department of Engineering, University of Cambridge, Cambridge, United Kingdom.*
[2] *School of Information Science and Technology, ShanghaiTech University, Shanghai, China.*
[3] *School of Electrical Engineering, Shandong University, Jinan, China.*
Email: smg84@cam.ac.uk

***Abstract*—This paper develops an inductive power transfer (IPT) system with stable output power based on a Class E/EF inverter. Load-independent design of Class E/EF inverter has recently attracted widespread interest. However, applying this design to IPT systems has proven challenging when the coupling coefficient is weak. To solve this issue, this paper uses an expanded impedance model and substitutes the secondary side's perfect resonance with a detuned design. Therefore, the system can maintain stable output even under a low coupling coefficient. A 400 kHz experimental prototype validates these findings. The experimental results indicate that the output power fluctuation remains within 15% as the coupling coefficient varies from 0.04 to 0.07. The peak power efficiency achieving 91%.**

***Index Terms*—Class E/EF inverter, Stable output, extended impedance method**

I. Introduction

In recent years, inductive wireless power transfer technology has conquered various fields and demonstrated its versatility and applicability across diverse sectors. Unlike conventional charging methods that offer robust wired connections and generally reliable power transfer [1]–[19], inductive power transfer (IPT) systems are inherently sensitive to coupling, which means that any variations in the coupling coefficient between the transmitter and the receiver can cause significant fluctuation in the output power. The power fluctuation can impact the efficiency and stability of the power transfer process. Consequently, the establishment of an IPT system that is robust against coupling variations, capable of maintaining consistent and reliable power transfer despite changes in coupling conditions, is crucial for advancing inductive power transfer technology and ensuring its widespread adoption and success in various applications [20]–[27].

The single switch Class E / EF inverter has attracted widespread application across various industries and applications due to its exceptional cost-effectiveness and high operational efficiency [28]–[31]. However, the intrinsic load sensitivity of resonant converters poses significant challenges when feeding wireless power transfer systems. Consequently, a load-independent design of the class E / EF inverter seems to constitute a promising solution to overcome the challenge [32]. However, the implementation of a load-independent Class E / EF inverter is restricted by a minimum resistance requirement [32]. This means that the inverter must be connected to a load with a resistance that is above a certain threshold to ensure stable and efficient operation. When deployed within an IPT system, based on the reflected impedance model, there is an inherent lower bound on the coupling coefficient that must be met to maintain stable power. Given that the majority of IPT systems operate under weak coupling, this seemingly optimal scheme harbors substantial limitations.

This study comprehensively analyses and solves the critical failure of load-independent design in Class E/EF driven IPT systems when they are operating under weak coupling conditions. In response, we propose an innovative solution by substituting the ideal resonance on the secondary side with a detuned design. This detuned design incorporates an expanded impedance model [33], [34] to further explore the potential. This paper found that when the reflection impedance shifts from resistive to capacitive, it can effectively counteract the destabilizing effects of weak coupling. Moreover, this paper further elucidate theoretically why an inductive nature is more favorable for stable output in IPT systems.

II. Topology of Class-E/EF Inverter Based IPT System

Fig 1(a) depicts the topology of a basic IPT system driven by a Class E inverter. V_{dc} is the input voltage. S is the switch, whose duty cycle is D and frequency is f_s. The TX coil's self inductance L_{tx} would resonate with C_0 at frequency f_s with additional reactance X. Please note that L_{tx} will resonate with C_0 directly, which is different from a traditional resonate tank. In contrast to the traditional Class E inverter, L_1 serves as a resonant inductor in place of a choke. The resonance frequency between L_1 and C_1 could be normalized with respect to w_s; a frequency factor q is then defined as

$$X = \omega_s L_{tx} - 1/(\omega_s C_0), \tag{1}$$

$$q = 1/\left(\omega_s \sqrt{L_1 C_1}\right). \tag{2}$$

Meanwhile, Fig. 1(b) illustrates the topology of the IPT system driven by the Class EF inverter, where the input inductor L_f serves as an RF choke. C_1 is a shunt capacitor that absorbs the switch junction capacitance. At f_s, L_0 and

This work was supported by National Natural Science Foundation of China under Grant 52477013 and Lingang Laboratory under Grant NO. LG-GG-202402-06-10.

C_0 resonate with the additional reactance X_0. The shunt tank L_2 and C_2 would resonate at f_2, which can be described as

$$X_0 = \omega_s L_{tx} - 1/(\omega_s, C_0) \tag{3}$$

$$f_2 = 1/\left(2\pi\sqrt{L_2 C_2}\right). \tag{4}$$

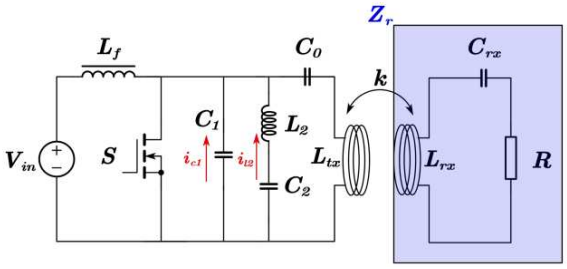

(a)

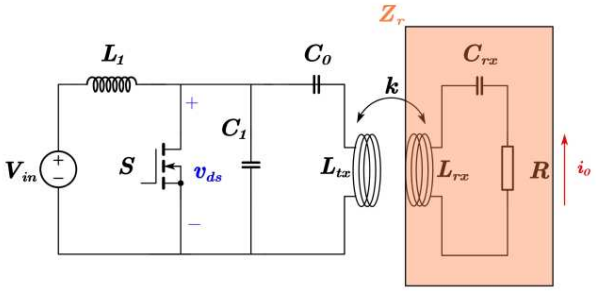

(b)

Fig. 1: Circuit model. (a) Basic IPT system driven by class EF inverter. (b) Basic IPT system driven by class E inverter.

III. Design Methodology

A. Load-independent Class-E inverter

When the quality factor Q is high, the output current i_0 and voltage across the switch v_{ds} can obtained as follows with β and p as given:

$$i_o(\omega t) = I_m \sin(\omega t + \phi) \tag{5}$$

$$\frac{\nu_{\rm DS}(\omega t)}{V_{\rm in}} = \frac{I_m}{\omega C_1 V_{\rm in}} \int_{2\pi D}^{\omega t} \frac{i_{C_1}(\tau)}{I_m} d\tau = q^2 p \beta(\omega t) \tag{6}$$

$$\beta(\omega t) = \int_{2\pi D}^{\omega t} \frac{i_{C_1}(\omega t)}{I_m} d\omega t, p = \frac{\omega L_1 I_m}{V_{\rm in}} \tag{7}$$

The switch voltage is filtered by the total impedance of j_X and Z_r. Consequently, upon applying the Fourier transform to v_{ds}, its sine and cosine components are respectively applied to the resistive and reactive parts of the entire branch, i.e.,

$$\begin{aligned} \frac{\nu_{Z_r}}{V_{\rm in}} &= \frac{1}{\pi} \int_{2\pi D}^{2\pi} \frac{\nu_{\rm ds}(\omega t)}{V_{\rm in}} \sin(\omega t + \phi) d\omega t \\ &= \frac{q^2 p}{\pi} \int_{2\pi D}^{2\pi} \beta(\omega t) \sin(\omega t + \phi)\, d\omega t = \frac{q^2 p}{\pi} \psi_1, \end{aligned} \tag{8}$$

$$\begin{aligned} \frac{\nu_{jX}}{V_{\rm in}} &= \frac{1}{\pi} \int_{2\pi D}^{2\pi} \frac{\nu_{\rm ds}(\omega t)}{V_{\rm in}} \cos(\omega t + \phi) d\omega t \\ &= \frac{q^2 p}{\pi} \int_{2\pi D}^{2\pi} \beta(\omega t) \cos(\omega t + \phi) d\omega t = \frac{q^2 p}{\pi} \psi_2. \end{aligned} \tag{9}$$

There are two design objectives: Constant ZVS and constant output, which can be derived as

$$\frac{\partial}{\partial p}\left(\frac{q^2 p}{\pi}\psi_1\right) = \frac{q^2}{\pi}\frac{\partial p \psi_1}{\partial p} = 0 \text{ over range of } p, \tag{10}$$

$$\beta(2\pi) = 0 \text{ over } \mathbb{D}_p. \tag{11}$$

Therefore, the design variable can be obtained as

$$\frac{\nu_{jX}}{V_{\rm in}} = \frac{q^2 p}{\pi}\psi_2(q, p, \phi, D) = \frac{i_m X}{V_{\rm in}} = p\frac{X}{\omega L_1}, \tag{12}$$

$$\frac{X(q, \phi, D)}{\omega L_1} = \frac{q^2}{\pi}\psi_2(q, \phi, D) \tag{13}$$

The solution of above equation is q=1.2915, $\frac{X(q,\phi,D)}{\omega L_1} = 0.2663$.

B. Load-independent Class-EF inverter

Beginning with the series $L_2\,C_2$ network, its current can obtained as

$$\frac{i_{L_2}}{I_{\rm in}}(\omega t) = A_2 \cos(q_2 \omega t) + B_2, \tag{14}$$

$$\sin(q_2 \omega t) - \frac{q_2^2 p}{q_2^2 - 1}\sin(\omega t + \phi) + \frac{1}{k+1}, \tag{15}$$

$$k = \frac{C_1}{C_2}, q_2 = \frac{1}{\omega}\sqrt{\frac{C_1 + C_2}{L_2 C_1 C_2}} = q_1\sqrt{\frac{k+1}{k}}, \tag{16}$$

$$p = \frac{C_2}{C_1 + C_2}\frac{I_m}{I_{\rm in}} = \frac{1}{k+1}\frac{I_m}{I_{\rm in}}, \tag{17}$$

where k, q_2, p can be obtained from (16) and (17).

Meanwhile, the current flow into C_1 and the drain voltage follow

$$\frac{i_{C_1}}{I_{\rm in}}(\omega t) = 1 - p(k+1)\sin(\omega t + \phi) - \frac{i_{L_2}}{I_{\rm in}}(\omega t), \tag{18}$$

$$\frac{\nu_{\rm ds}(\omega t)}{V_{\rm in}} = 2\pi\frac{\beta(\omega t)}{\alpha}, \tag{19}$$

$$\beta(\omega t) = \int_{2\pi D}^{\omega t} \frac{i_{C_1}}{I_{\rm in}}(\tau) d\tau, \tag{20}$$

$$\alpha = \int_{2\pi D}^{2\pi} \beta(\omega t) d\omega t. \tag{21}$$

Similar to the Class-E design, the Fourier transform yields

$$\begin{aligned} \frac{\nu_{Z_r}}{V_{\rm in}} &= \frac{2}{\alpha}\int_{2\pi D}^{2\pi} \beta(\omega t)\sin(\omega t + \phi) d\omega t = \frac{2}{\alpha}\psi_1, \\ \frac{\nu_{jX}}{V_{\rm in}} &= \frac{2}{\alpha}\int_{2\pi D}^{2\pi} \beta(\omega t)\cos(\omega t + \phi) d\omega t = \frac{2}{\alpha}\psi_2. \end{aligned} \tag{22}$$

There are also two design objectives: Constant ZVS and constant output power per

$$\frac{\partial}{\partial p}\left(p\frac{\psi_1(p)}{\alpha(p)}\right)=0 \quad \text{over } \mathbb{D}_p, \tag{23}$$

$$\beta(2\pi)=0 \quad \text{over } \mathbb{D}_p. \tag{24}$$

Therefore, the design variable can be obtained as

$$\frac{1}{\omega R_L C_1}=\frac{\pi p^2(k+1)^2}{\alpha(p)}, \tag{25}$$

$$\omega X C_1=\frac{1}{\pi p(k+1)}\psi_2\big(q_1,k,\phi,D\big), \tag{26}$$

$$I_m=2\frac{\psi_1(p)}{\alpha(p)}\frac{V_{\text{in}}}{R}. \tag{27}$$

The solution of above equation is q=1.3, $\frac{X(q,\phi,D)}{\omega L_1}=0.3533$.

C. Detuned Compensation Design

As mentioned before, this design has the minimum coupling-variation requirement. In scenarios with low coupling coefficients, the detuned secondary design allows for the full release of design variables.

1) Expanded impedance model: To employ the expanded impedance model, the initial step involves representing circuit elements through their respective impedance matrices. Define the critical harmonic order range as $[-N,N]$, where harmonics outside this range are disregarded. It is crucial to set this range to optimize computational efficiency without compromising design accuracy. Consequently, all impedance expressions form square matrices of dimension $(2N+1)$. Notably, resistors, inductors, and capacitors are represented by diagonal matrices.

The matrix form of a resistor follows

$$\mathbf{Z_R}=\begin{bmatrix} R & \cdots & 0 & \cdots & 0\\ \vdots & \ddots & \ddots & \ddots & \vdots\\ 0 & \ddots & R & \ddots & 0\\ \vdots & & & & \\ \vdots & \ddots & \ddots & \ddots & \vdots\\ 0 & \cdots & 0 & \cdots & R \end{bmatrix}, \tag{28}$$

the matrix form of inductors equivalently

$$\mathbf{Z_L}=\begin{bmatrix} -jN\omega L & \cdots & 0 & \cdots & 0\\ \vdots & \ddots & \ddots & \ddots & \vdots\\ 0 & \ddots & 0 & \ddots & 0\\ \vdots & \ddots & \ddots & \ddots & \vdots\\ 0 & \cdots & 0 & \cdots & jN\omega L \end{bmatrix}. \tag{29}$$

The matrix form of capacitors follows

$$\mathbf{Z_C}=\begin{bmatrix} -jN\omega C & \cdots & 0 & \cdots & 0\\ \vdots & \ddots & \ddots & \ddots & \vdots\\ 0 & \ddots & 0 & \ddots & 0\\ \vdots & \ddots & \ddots & \ddots & \vdots\\ 0 & \cdots & 0 & \cdots & jN\omega C \end{bmatrix}^{-1}. \tag{30}$$

The transistor is modeled as a resistance that varies with time, featuring a significant OFF-state resistance R_{off} and a minor ON-state resistance R_{on}. This applies to all harmonic orders p within the range $[-N,N]$.

$$R_{S,p}=\begin{cases} R_{\text{ON}}D+R_{\text{OFF}}(1-D), & p=0\\ R_{\text{ON}}-R_{\text{OFF}}\frac{\sin(p\pi D)}{p\pi}e^{-jp\pi D}, & p\neq 0 \end{cases}. \tag{31}$$

Note that D is the duty cycle of the driving signal. The impedance expression of the active switch is

$$\mathbf{Z}_{\text{S}}=\begin{bmatrix} R_{S,0} & \cdots & R_{S,-N} & \cdots & R_{S,-2N}\\ \vdots & \ddots & \ddots & \ddots & \vdots\\ R_{S,N} & \ddots & R_{S,0} & \ddots & R_{S,-N}\\ \vdots & \ddots & \ddots & \ddots & \vdots\\ R_{S,2N} & \cdots & R_{S,N} & \cdots & R_{S,0} \end{bmatrix}. \tag{32}$$

The dc input voltage can be expressed as

$$\mathbf{V}_{in}=\begin{bmatrix} 0 & \cdots & 0 & V_{\text{in}} & 0 & \cdots & 0 \end{bmatrix}^{\text{T}}. \tag{33}$$

Besides simulating the steady-state waveforms, the supplied power and load power at steady state can also be derived as

$$\begin{aligned} \bar{P}_{\text{in}} &= \frac{1}{T}\int_T |V_{\text{DC}}(t)i_0(t)|\,\mathrm{d}t\\ &= \sum_{k=-\infty}^{+\infty} V_{\text{DC},k}I_{0,k}\\ &= \mathbf{V}_{\mathbf{DC}}^{\text{T}}\mathbf{Y}_{\mathbf{Class-E}}\mathbf{V}_{\mathbf{DC}},\\ \bar{P}_{\text{out}} &= \mathbf{V}_{\mathbf{C}}^{\text{T}}\mathbf{Y}_{\text{load}}\,\mathbf{V}_{\mathbf{C}}. \end{aligned} \tag{34}$$

2) Analysis Results: As depicted in Fig. 2, this work uses an expanded impedance model. For the specific topology, determined values, and given range of k, we can calculate the power drop ratio β, and by select minimum β, can get the candidate points, which are listed in TABLE I.

TABLE I: Parameters and constraint condtions of design.

Parameters	Value	Parameters	Value
L_1	10 μH	V_{in}	30 V
L_{tx}	140 μH	L_{rx}	50 μH
R_L	12.5 Ω	C_0	1.15 nF
C_1	9.49 nF	C_{rx}	3.3 nF
Q_{tx}	350	Q_{rx}	251

The selected design point reveals an inductive characteristic on the secondary side. This occurs because an inductive secondary side results in a capacitive impedance when reflected to

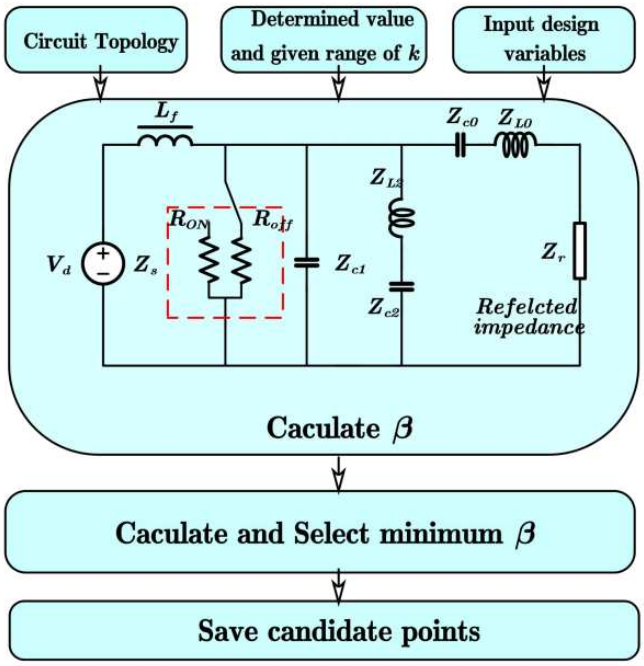

Fig. 2: Design flow chat

the primary side. Within a load-independent design framework, even in scenarios where low coupling leads to performance degradation, the voltage at the switching node remains relatively constant. Consequently, if the reflected impedance to the primary side is capacitive, it can compensate for a portion of the transmitter coil's impedance and secure a larger share of the voltage, thereby facilitating the maintenance of a stable output.

IV. Simulation Results

The point selection model does not account for the effects of parasitic resistances and the nonlinear junction capacitance. Therefore, additional validation through simulation is necessary to confirm the model's effectiveness. Using the parameters of Table I, the quality factors of the inductive components are taken into consideration, and the switch is modeled with a Spice model with the GaN transistor GS66508B.

Fig. 3 illustrates the relationship between output power and varying k. It demonstrates that for $k < 0.05$, P_0 increases with k, whereas for $k > 0.05$, P_0 decreases with k. In this context, β is 20%.

Fig. 4 presents the waveform of the voltage across the switch v_{ds}. It can be observed that under this design, ZVS only holds true for certain coupling coefficients. However, this does not necessarily imply an ineffective design, as the core objective of this paper is to achieve stable output, and constant ZVS is not the primary design goal. On the other hand, the implementation of ZVS aims to achieve high efficiency. Section V describes the experimental verification to demonstrate that this design, even with partial loss of ZVS, can still maintain high efficiency.

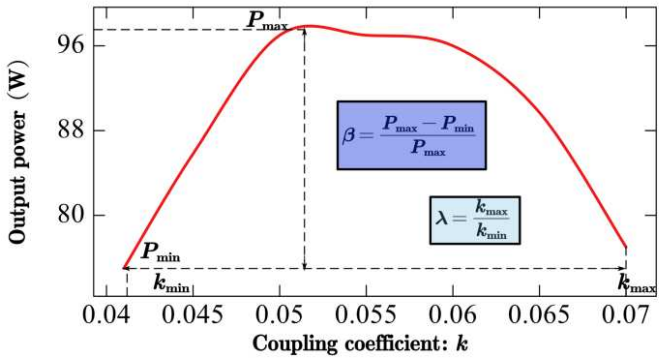

Fig. 3: k-dependent power under proposed design.

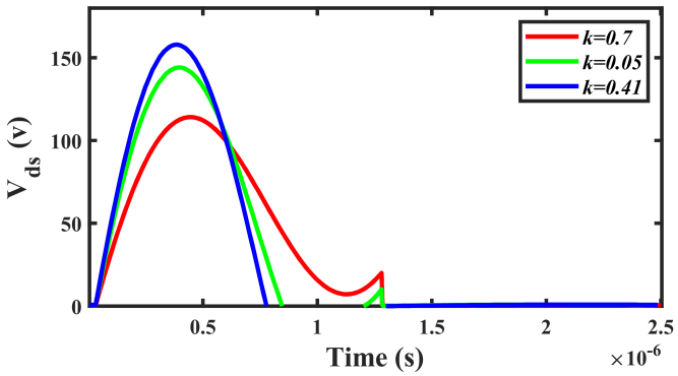

Fig. 4: v_{ds} under different k.

V. Experimental Results

An experimental IPT system, designed as previously described, is depicted in Fig. 7. Both the TX and RX coils are crafted from Litz wire, with specifications of 0.1 mm by 150 strands and a diameter of 1.7 mm. All system parameters are detailed in Table I. The circuit uses high-precision, high-quality-factor NP0/C0G ceramic capacitors. The system employs a GaN-based transistor (GS66508B). It is important to note that a constant switch junction capacitance of 200 pF is taken into account and is to be incorporated into C_1. Fig. 5 demonstrates an experimental IPT system.

Fig. 5 graphs typical waveforms for different coupling conditions. It furthermore displays the measured output power and efficiency. The power fluctuation rate β is 15% which successfully aligning with the predictions made by the model-based design. It can also be observed that as the coupling coefficient increases, the efficiency gradually improves. Although partial ZVS is lost, an efficiency above 85% is still maintained, which verifies the feasibility of the design.

VI. Conclusions

This work solves the shortcomings of load-independent Class E/EF designs when subjected to low coupling variations. A detuned design on the secondary side can liberate global variables. Analysis with an expanded impedance model identifies the optimal design points. Experimental results indicate that under low coupling conditions, the power fluctuation rate

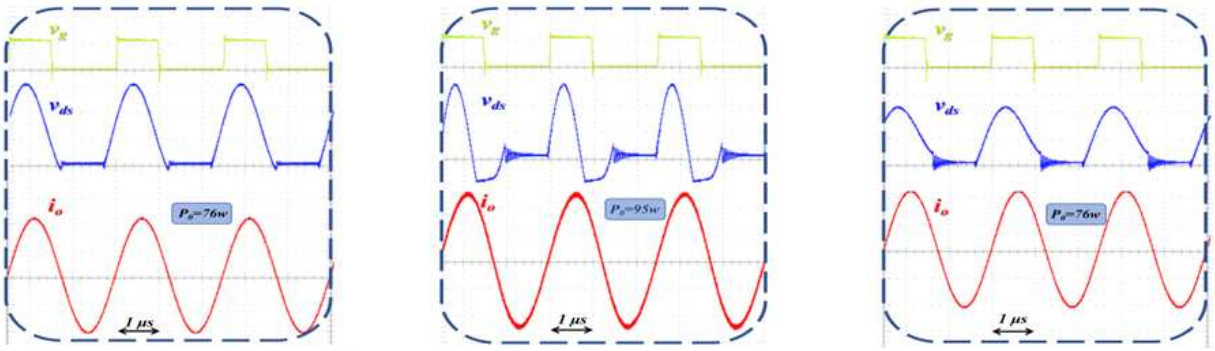

Fig. 5: Waveform at different k: v_g (5V/div), v_{ds} (50V/div), i_0 (2A/div). (a) k = 0.04. (b) k = 0.05. (c) k = 0.07.

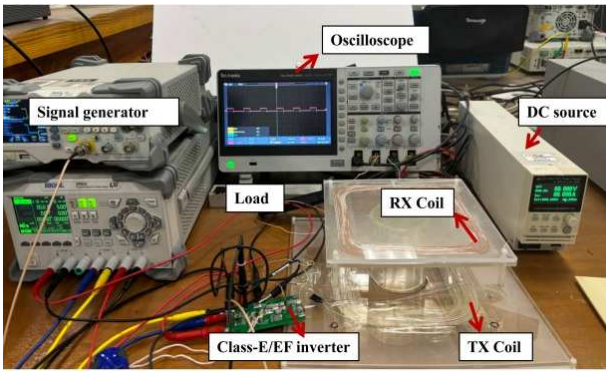

Fig. 6: Experimental setup.

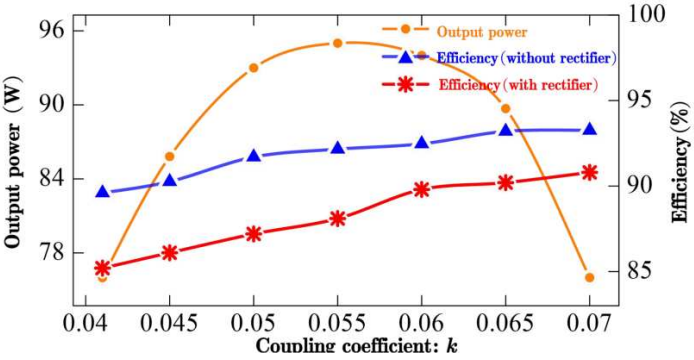

Fig. 7: Output power and efficiency.

remains at 15%, with efficiency maintained within the range of 86–91% as the coupling coefficient k varies from 0.04 to 0.07.

REFERENCES

[1] H. Wang, N. Tashakor, W. Jiang, W. Liu, C. Q. Jiang, and S. M. Goetz, "Hacking encrypted frequency-varying wireless power: Cyber-security of dynamic charging," *IEEE Transactions on Energy Conversion*, vol. 39, no. 3, pp. 1947–1957, 2024.

[2] S. Liu, Y. Wu, L. Zhou, R. Mai, Z. He, and S. M. Goetz, "A two-dimensional misalignment-tolerant ipt system based on three-arm voltage doubler rectifier," in *2022 IEEE Energy Conversion Congress and Exposition (ECCE)*, 2022, pp. 1–7.

[3] H. Wang, K. T. Chau, W. Liu, and S. M. Goetz, "Design and control of wireless permanent-magnet brushless dc motors," *IEEE Transactions on Energy Conversion*, vol. 38, no. 4, pp. 2969–2979, 2023.

[4] X. Yang, J. Li, K. Wang, U. Kim, Z. Zhang, and K.-B. Park, "A weighting factor design approach for fcs-mpc techniques based on pso and k-means algorithm," in *2022 IEEE Energy Conversion Congress and Exposition (ECCE)*, 2022, pp. 1–8.

[5] Z. Wu, H. Han, J. Lin, S. Xie, Y. Sun, Z. Tang, and F. Blaabjerg, "Admittance-based stability analysis of resistance-emulating controlled grid-connected voltage source rectifiers," *IEEE Transactions on Industrial Electronics*, vol. 70, no. 10, pp. 10 076–10 088, 2023.

[6] S. Ni, C. Li, and Z. Zheng, "Control strategy of a hybrid sic-si traction inverter for direct-drive multiphase pmsms in marine propulsion," *IEEE Transactions on Power Electronics*, vol. 39, no. 12, pp. 16 400–16 414, 2024.

[7] Z. Wei, H. Wang, Y. Lu, D. Shu, G. Ning, and M. Fu, "Bidirectional constant current string-to-cell battery equalizer based on l2c3 resonant topology," *IEEE Transactions on Power Electronics*, vol. 38, no. 1, pp. 666–677, 2023.

[8] M. Lu, M. Qin, W. Mu, J. Fang, and S. M. Goetz, "A hybrid gallium-nitride–silicon direct-injection universal power flow and quality control circuit with reduced magnetics," *IEEE Transactions on Industrial Electronics*, vol. 71, no. 11, pp. 14 161–14 174, 2024.

[9] M. Lu, M. Qin, J. Kacetl, E. Suresh, T. Long, and S. M. Goetz, "A novel direct-injection universal power flow and quality control circuit," *IEEE Journal of Emerging and Selected Topics in Power Electronics*, vol. 11, no. 6, pp. 6028–6041, 2023.

[10] X. Huang, Y. Kong, Z. Ouyang, W. Chen, and S. Lin, "Analysis and comparison of push–pull class-e inverters with magnetic integration for megahertz wireless power transfer," *IEEE Transactions on Power Electronics*, vol. 35, no. 1, pp. 565–577, 2020.

[11] H. Sekiya, K. Tokano, W. Zhu, Y. Komiyama, and K. Nguyen, "Design procedure of load-independent class-e wpt systems and its application in robot arm," *IEEE Transactions on Industrial Electronics*, vol. 70, no. 10, pp. 10 014–10 023, 2023.

[12] C. H. Lee, G. Jung, K. A. Hosani, B. Song, D.-k. Seo, and D. Cho, "Wireless power transfer system for an autonomous electric vehicle," in *2020 IEEE Wireless Power Transfer Conference (WPTC)*, 2020, pp. 467–470.

[13] Z. Yue, Q. Zhang, Z. Yang, R. Bian, D. Zhao, and B.-Z. Wang, "Wall-meshed cavity resonator-based wireless power transfer without blocking wireless communications with outside world," *IEEE Transactions on Industrial Electronics*, vol. 69, no. 7, pp. 7481–7490, 2022.

[14] M. Venkatesan, R. Narayanamoorthi, K. M. AboRas, and A. Emara, "Efficient bidirectional wireless power transfer system control using dual phase shift pwm technique for electric vehicle applications," *IEEE Access*, vol. 12, pp. 27 739–27 755, 2024.

[15] T. Mishima and C.-M. Lai, "Zero-phase-angle load-independent and -adaptable dual-side lcc inductive wireless power transfer system," *IEEE Transactions on Transportation Electrification*, vol. 10, no. 2, pp. 3492–3503, 2024.

[16] D.-W. Seo, J.-H. Lee, and H.-S. Lee, "Optimal coupling to achieve maximum output power in a wpt system," *IEEE Transactions on Power Electronics*, vol. 31, no. 6, pp. 3994–3998, 2016.

[17] T. Fujita, T. Yasuda, and H. Akagi, "A dynamic wireless power transfer system applicable to a stationary system," *IEEE Transactions on Industry Applications*, vol. 53, no. 4, pp. 3748–3757, 2017.

[18] F. Lu, H. Zhang, H. Hofmann, and C. C. Mi, "An inductive and capacitive combined wireless power transfer system with lc-compensated topology," *IEEE Transactions on Power Electronics*, vol. 31, no. 12, pp. 8471–8482, 2016.

[19] D. Ahn and P. P. Mercier, "Wireless power transfer with concurrent 200-khz and 6.78-mhz operation in a single-transmitter device," *IEEE Transactions on Power Electronics*, vol. 31, no. 7, pp. 5018–5029, 2016.

[20] L. Gu and J. Rivas-Davila, "1.7 kw 6.78 mhz wireless power transfer with air-core coils at 95.7% dc–dc efficiency," in *2021 IEEE Wireless Power Transfer Conference (WPTC)*, 2021, pp. 1–4.

[21] L. Gu, W. Liang, and J. R. Davila, "Design of very-high-frequency synchronous resonant dc-dc converter for variable load operation," in *2017 IEEE Energy Conversion Congress and Exposition (ECCE)*, 2017, pp. 3447–3454.

[22] X. Tian, W. Liu, K. T. Chau, and S. M. Goetz, "Omnidirectional magnetic resonant extender design for underwater wireless charging system," *IEEE Journal of Emerging and Selected Topics in Power Electronics*, vol. 12, no. 4, pp. 3325–3333, 2024.

[23] M. Liu and M. Chen, "Dual-band wireless power transfer with reactance steering network and reconfigurable receivers," *IEEE Transactions on Power Electronics*, vol. 35, no. 1, pp. 496–507, 2020.

[24] X. Tian, J. Zhang, H. Wang, and S. M. Goetz, "Design and analysis of automatic modulation and demodulation strategy in wireless power and drive transfer system," *IEEE Transactions on Industrial Electronics*, 2024.

[25] P. Zhao, J. Liang, H. Wang, and M. Fu, "Detuned lcc/ss compensation for stable-output inductive power transfer system under ultra-wide coupling variation," *IEEE Transactions on Power Electronics*, 2023.

[26] H. Feng, T. Cai, S. Duan, X. Zhang, H. Hu, and J. Niu, "A dual-side-detuned series–series compensated resonant converter for wide charging region in a wireless power transfer system," *IEEE Trans. Ind. Electron.*, vol. 65, no. 3, pp. 2177–2188, 2018.

[27] H. Feng, A. Dayerizadeh, and S. M. Lukic, "A coupling-insensitive x-type ipt system for high position tolerance," *IEEE Trans. Ind. Electron.*, vol. 68, no. 8, pp. 6917–6926, 2021.

[28] J. Xu, Z. Tong, and J. Rivas-Davila, "1 kw mhz wideband class E power amplifier," *IEEE Open Journal of Power Electronics*, vol. 3, pp. 84–92, 2022.

[29] K. Surakitbovorn and J. M. Rivas-Davila, "A simple method to combine the output power from multiple class-e power amplifiers," *IEEE Journal of Emerging and Selected Topics in Power Electronics*, vol. 10, no. 2, pp. 2245–2253, 2022.

[30] Z. Tong and J. M. Rivas-Davila, "Wideband push-pull class e amplifier for rf power delivery," in *2023 IEEE 24th Workshop on Control and Modeling for Power Electronics (COMPEL)*, 2023, pp. 1–7.

[31] S. Liu, M. Liu, S. Yang, C. Ma, and X. Zhu, "A novel design methodology for high-efficiency current-mode and voltage-mode class-e power amplifiers in wireless power transfer systems," *IEEE Transactions on Power Electronics*, vol. 32, no. 6, pp. 4514–4523, 2017.

[32] S. Aldhaher, D. C. Yates, and P. D. Mitcheson, "Load-independent class e/ef inverters and rectifiers for mhz-switching applications," *IEEE Transactions on Power Electronics*, vol. 33, no. 10, pp. 8270–8287, 2018.

[33] Y. Jiang, H. Li, Y. Liu, J. Liang, H. Wang, and M. Fu, "Multiconstraint design of single-switch resonant converters based on extended impedance method," *IEEE Journal of Emerging and Selected Topics in Power Electronics*, vol. 11, no. 2, pp. 1901–1912, 2023.

[34] J. Liang and W.-H. Liao, "Steady-state simulation and optimization of class-e power amplifiers with extended impedance method," *IEEE Transactions on Circuits and Systems I: Regular Papers*, vol. 58, no. 6, pp. 1433–1445, 2011.